ACS APPLIED MATERIALS & INTERFACES

www.acsami.org Research Article

Conversion of Biomasses and Copper into Catalysts for Photocatalytic CO_2 Reduction

Zhuofeng Hu* and Weiwei Liu

Cite This: ACS Appl. Mater. Interfaces 2020, 12, 51366−51373 Read Online

ACCESS | Metrics & More | Article Recommendations | Supporting Information

Downloaded via UNIV INDUSTRIAL DE SANTANDER on November 18, 2020 at 14:55:55 (UTC).
See https://pubs.acs.org/sharingguidelines for options on how to legitimately share published articles.

ABSTRACT: The rapid increase of CO_2 in the atmosphere has caused serious environmental problems. Burning of biomass wastes increases the content of CO_2 in the environment. Herein, we propose a new strategy to convert biomass into photocatalysts for artificial CO_2 reduction. Using a hydrothermal method, carbohydrates from biomass can be converted into hydrothermal carbonaceous carbon (HTCC). The HTCC consists of plenty of sp^2-hybridized structures, which are capable of absorbing solar light for photocatalytic CO_2 reduction. Furthermore, with the addition of Cu cocatalysts, higher activity can be obtained for CO_2 reduction. The activity of Cu-HTCC is 32 and 1.7 times higher than that of commercial TiO_2 and pure HTCC, respectively. This method provides a new strategy of trash to treasure, which converts biomass waste into photocatalysts for CO_2 reduction.

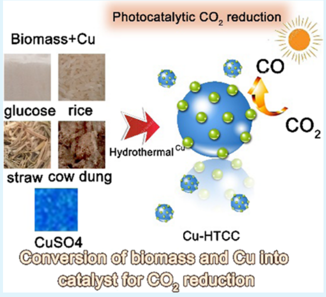

KEYWORDS: *biomass, CO_2 reduction, copper, hydrothermal carbonaceous carbon, glucose, straw*

INTRODUCTION

The rapid increase of CO_2 in the atmosphere has become one of the hot issues for human beings.[1−4] According to the report of the National Oceanic and Atmospheric Administration (NOAA), the content of CO_2 in the atmosphere has reached a record-high level of about 415 ppm. As reported by the World Meteorological Organization (WMO), the content of CO_2 in the atmosphere exhibits an increment of 46% related to that in the 1900s. Such a rapid increase in CO_2 has caused serious global warming.[5−9] It has been reported that the rise in average air temperature nowadays is by 0.8 °C compared with that at the beginning of the 20th century. The extreme high temperature in the past summer affected several regions on the world. In Europe and China, air temperature remained at a high level of >39 °C for several days and caused the death of some citizens. In the Amazon rainforest area, forest fires induced by high temperatures occur more and more frequently.

Living biomasses of plants are one of the most important resources to reduce CO_2 via photosynthesis.[10,11] However, plants after death leave plenty of biomass waste and they can no longer reduce CO_2. Agriculture and graziery in the country produce plenty of biomass waste every year. However, nowadays, many biomasses are simply burned to generate heat, especially in rural areas. This oppositely releases the fixed carbon into the greenhouse gas of CO_2. Other harmful matter like oxynitride, aldehyde, methylbenzene, haze, PM2.5 particles, and metal or metal oxide particles are also produced. This aggravates global warming and causes serious environmental problems.[5−9,12−15] Conversion of biomass into valuable products is hence of great significance. The ever-increasing environmental problems have stimulated scientists to develop new methods to utilize biomasses more efficiently.

Artificial reduction of CO_2 into valuable HCOOH, CH_3OH, CO, and CH_4 is another effective approach to utilize CO_2. However, the carbon in CO_2 is at its highest oxidation state (C^{4+}) and the CO_2 molecule is very stable. Traditionally, high temperature or high voltage is often needed to achieve the reduction of CO_2. Recently, the photocatalytic reduction of CO_2 has received extensive attention. Using sustainable and clean solar energy, CO_2 can be reduced under mild conditions. This method is safe and sustainable and has been generally accepted as a promising method to reduce CO_2.[8,12,13,15]

Carbon-based photocatalysts are one kind of hot materials used for photocatalytic H_2 evolution, pollutant degradation, and CO_2 reduction because they are abundant, easily accessible, and environmentally friendly.[16−19] Carbonaceous semiconductors like g-C_3N_4, rGO, and GO are important materials for photocatalytic reduction of CO_2. They are inexpensive and have the potential to achieve a process practically feasible to CO_2 reduction. They often have a suitable band diagram with regard to photocatalytic CO_2 reduction. Their layer structure plays an important role in photoreduction of CO_2. Besides, they are easy to couple with other semiconductors with a proper band diagram or by dispersing plasmonic nano metals to create a heterojunction,

Received: July 24, 2020
Accepted: October 21, 2020
Published: November 6, 2020

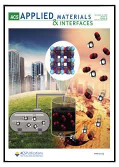

ACS Publications © 2020 American Chemical Society

https://dx.doi.org/10.1021/acsami.0c13323
ACS Appl. Mater. Interfaces 2020, 12, 51366−51373

which can greatly improve the activity. Therefore, developing high-efficiency carbonaceous semiconductors is very important for photocatalytic CO_2 reduction.[19]

Biomass is one of the most wide spread carbon materials on earth. However, raw biomass hardly exhibits appreciable artificial photocatalytic activity. Recently, a method to convert biomass into photocatalysts has been reported.[20,21] Carbohydrates from biomass can be converted into hydrothermal carbonaceous carbon (HTCC). Many biomasses contain carbohydrates. The HTCC consists of plenty of sp^2-hybridized structures, which are capable of absorbing solar light for photocatalytic dye degradation and disinfection.[21−23] For example, Zhang's group prepared HTCC for the degradation of sulfadimidine.[24,25] However, this kind of HTCC material has never been reported for CO_2 reduction.

Herein, considering the difficulty of treating a large number of biomass wastes and the CO_2-induced global warming, we propose a strategy to convert biomass waste into HTCC for photocatalytic CO_2 reduction. Our goal is to propose a new approach for the resource utilization of biomass waste. Therefore, biomass can not only reduce CO_2 when they are alive but can also photocatalytically reduce CO_2 via transforming into HTCC.

Besides, it is well known that metals have a lower Fermi level than an n-type semiconductor, and metals often exhibit high activity in a catalytic reaction due to their d-band electrons. In the CO_2 reduction, addition of metals can help to improve the activity. In our experiment, we choose Cu metal as a cocatalyst partially because it often exhibits good activity in CO_2 reduction and because its redox potential is relatively positive (0.3419 V vs RHE). This makes it easy to be reduced into elemental Cu under hydrothermal conditions. In our experiment, when a heavy metal ion of Cu is introduced in the synthesis, it can be fixed, collected, and reduced into metal Cu in the HTCC to produce a Cu-HTCC photocatalyst. It can also be used as a photocatalyst for CO_2 reduction, and it exhibits 2-fold higher activity than pure HTCC. The products can convert CO_2 into CO with a generation rate between 148.8 and 643.5 μmol g^{-1} h^{-1}.

■ EXPERIMENTAL SECTION

Preparation of HTCC. Two grams of glucose was dissolved in 20 mL of distilled water. Subsequently, the solution was transferred to a 25 mL Teflon-lined stainless steel autoclave and heated at 180 °C for 8 h. After the reaction, the product was collected via centrifugation. After being washed with distilled water and ethanol several times, the product was dried in a vacuum oven at 90 °C for 24 h. In addition, biomasses of straw, rice (nonglutinous early season), and cow dung were also used as raw materials to prepare HTCC. All of the biomass was collected in the countryside of Kaiping city, Jiangmen district, Guangdong province, China.

Preparation of Cu-HTCC Composites. Glucose (2.0 g) and $CuSO_4$ (0.2 g) were dissolved in 20 mL of distilled water. Subsequently, the solution was transferred to a 25 mL Teflon-lined stainless steel autoclave and heated at 180 °C for 8 h. After the reaction, the product was collected via centrifugation. After being washed with distilled water and ethanol several times, the product was dried in a vacuum oven at 80 °C overnight. A biomass of straw was also mixed with $CuSO_4$ to prepare Cu-HTCC. Besides, Cu-HTCC was also prepared with glucose with a purity of 99.5, 98.0, and 96.0%.

Synthesis of C_3N_4. Two grams of melamine was heated at 600 °C for 2 h in an air atmosphere with a heating and cooling rate of 3 °C min^{-1}. The product was a yellow C_3N_4 powder.

Material Characterization. The morphology of the products was characterized by scanning electron microscopy (SEM) on an FEI Quanta 400 microscope and by transmission electron microscopy (TEM) on a CM-120 microscope (Philips, 120 kV) coupled with an energy-dispersive X-ray (EDS) spectrometer (Oxford Instrument). X-ray diffraction (XRD) was performed on a Rigaku SmartLab X-ray diffractometer using Cu Kα source irradiation (λ = 1.5406 Å). Thermogravimetric analysis (TG) was recorded on a DTA1700 (PE). The diffuse reflectance spectra (UV−vis) of the samples over a range of 300−2000 nm were recorded by a Hitachi U-4100 UV−vis system equipped with a Labsphere diffuse reflectance accessory. ^{13}C solid-state magic angle spinning (MAS) NMR experiments were acquired on a Bruker Avance 300 MHz (7 T) spectrometer using the 4 mm zirconia rotors as sample holders, spinning at an MAS rate v_{MAS} = 14 kHz. FT-IR spectra were recorded on a Perkin Elmer Frontier spectrometer on samples embedded in KBr pellets.

Photocatalytic CO_2 Reduction. The photocatalytic CO_2 reduction was carried out in a 100 mL home-made sealed glass reactor. TiO_2 P25 was used as a typical benchmark photocatalyst, which was purchased from Degussa from Germany. All of the samples were put into the reactor by the sampling procedure. Typically, 0.05 g of the photocatalysts (HTCC, TiO_2, or C_3N_4) was uniformly dispersed on a glass and put into the reactor. Briefly, the powder was dispersed in 1 mL of ethanol and ultrasonically treated for 2−3 min. Then, the suspension was drop-coated onto the glass substrate. When the sample was dried at room temperature, the glass substrate covered with the sample was put into the reaction. $KHCO_3$ (0.5 g) was also put into the reactor. The air in the reactor was removed by vacuuming the reactor. Then, 1 mL of 6 M HCl was injected into the reactor using a syringe injector. When HCl and $KHCO_3$ were reacted with each other thoroughly, the reactor was full of CO_2. A 300 W xenon lamp was used as the irradiation source. One milliliter of the gas was taken out at an interval of 0.5 h and measured by a Shimadzu GC 2014C gas chromatograph equipped with a flame ionization detector (FID) and a thermal conductivity detector (TCD). High-purity argon gas was used as a carrier gas. The GC curve showing the formation of CO and the standard curve are shown in Figures S1 and S2.

Photoelectrochemical Measurements. The powder samples were fabricated into electrodes on FTO glasses by electrophoretic deposition. Twenty milligrams of the powder sample was dispersed in 30 mL of acetone, and then 5 mg of iodine was introduced into the solution. The function of iodine is to induce a positive charge on the particles. Two glasses (FTO) at a distance of 1.5 cm apart were put in parallel in the suspension with an area of 1.5 × 1.5 cm^2 in the solution. Then, under 30 V of AC voltage, the sample particles were electrophoretically deposited on the FTO glasses. All of the photoelectrochemical measurements were performed in a three-electrode cell with a saturated potassium chloride silver chloride electrode (Ag/AgCl) as the reference electrode, a graphite rod (diameter 1.0 cm) as the counter electrode, and the HTCC or Cu-HTCC electrode as the working electrode. The electrolyte was 1 M $KHCO_3$ saturated with Ar or CO_2, which is often used to investigate the activity of CO_2 reduction for catalysts.[26,27] A 300 W xenon arc lamp coupled with an AM 1.5G global filter (100 mW cm^{-2}) and a UV cutoff filter (λ > 420 nm) were used as the irradiation source. Linear sweeps and transient photocurrent were measured by a CHI 760E electrochemical workstation.

Theoretical Calculations. VASP computational package was used for all of the calculations in this paper.[28] We applied the projector augmented-wave method with the Perdew−Burke−Ernzerhof GGA functional.[29−31] The electronic convergence limit was set to be 1×10^{-5} eV.[32] The optimization of atomic coordinates was considered to be converged if the Hellmann−Feynman force was smaller than 1×10^{-2} eV $Å^{-1}$. As the main photoactive component of HTCC is polyfuran, the HTCC slab consisting of four polyfuran chains is constructed. Each polyfuran is composed of six furan units. The vacuum region is about 10 Å in height. All atoms are relaxed during optimization. For the Cu-HTCC, a layer of Cu consisting of 17 Cu atoms is added on the top of the HTCC structure. To study the absorption energy, CO_2, CO, HCOOH, and a series of intermediates are introduced on the top of the HTCC structure.

Nanosecond Transient Absorption Spectroscopy. Ns-TA experiments were carried out using an EOS multichannel pump-probe transient absorption spectrometer (Ultrafast company). A Nd:YAG laser with a third harmonic process is used to produce the pump laser of 365 nm. A continuous light source is generated using a photonic crystal fiber with a range of 350−2250 nm. When the sample is excited by the pump light, the probe light passes through the sample and the absorption signal is detected by a fiber optic-coupled multichannel spectrometer with CMOS sensors with 2 nm intrinsic resolution.

■ RESULTS AND DISCUSSION

Structure and Morphology. Carbohydrates could be converted into HTCC microspheres (Figure S3) under hydrothermal conditions. They undergo a polymerization process and produce insolvable HTCC structures.[33−35] The HTCC contains some reducing functional groups.[36−39] Heavy metal ions can be fixed and encapsulated in the metal/HTCC composite. In the SEM images of Cu-HTCC, the HTCC particles are mainly spherical (Figures 1a and S3). In the TEM image focusing on the edge of the spheres, some 5−15 nm Cu particles are immobilized on the HTCC spheres. In the magnified HRTEM image, a Cu particle is clearly observed on the HTCC spheres (Figure 1b). The mapping images of C and O elements from the HTCC sphere and the mapping of the Cu element from the Cu nanoparticle all show uniform distribution (Figure S4). In the HRTEM image (Figure 1c,d), a lattice fringe with the d spacing of 0.209 is found, corresponding to the (111) facet of metal Cu, whereas the HTCC shows an amorphous structure (Figures 1d and S3), which is in good agreement with previous reports.[40] According to thermogravimetric (TG) analysis, the mass fraction of the Cu and HTCC is calculated to be 5.9 and 94.1 wt %, respectively (Section S1, Figure S5). The remaining content of Cu ions is measured by an inductive-coupled plasma (ICP) spectrometer and 98.4% of the Cu ions are reduced into Cu in the Cu-HTCC.

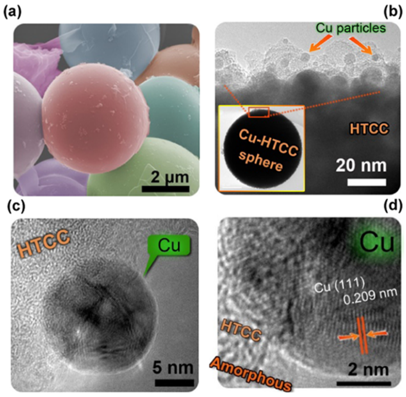

Figure 1. (a) Colored SEM. (b, c) TEM and (d) HRTEM images of Cu-HTCC prepared from glucose and $CuSO_4$. The inset in (b) is the TEM image of an individual Cu-HTCC particle.

The XRD pattern of Cu-HTCC presents three sharp diffraction peaks of metal Cu. Cu-HTCC exhibits peaks at 43.17, 50.42, and 74.10, which can be indexed as the (111), (200), and (220) diffraction planes of copper (JCPDS card no. 04-0836). The standard redox potential of Cu (Cu^{2+} + 2e = Cu, 0.339 V) is positive and it is easy to be reduced. In hydrothermal conditions, glucose acts as a reducing agent and reduces Cu ions into Cu metal nanoparticles. The positive value of 0.339 V indicates that Cu is easy to be reduced by reducing agents. HTCC does not show any diffraction peak in the XRD pattern due to its amorphous structure (Figure 2a).

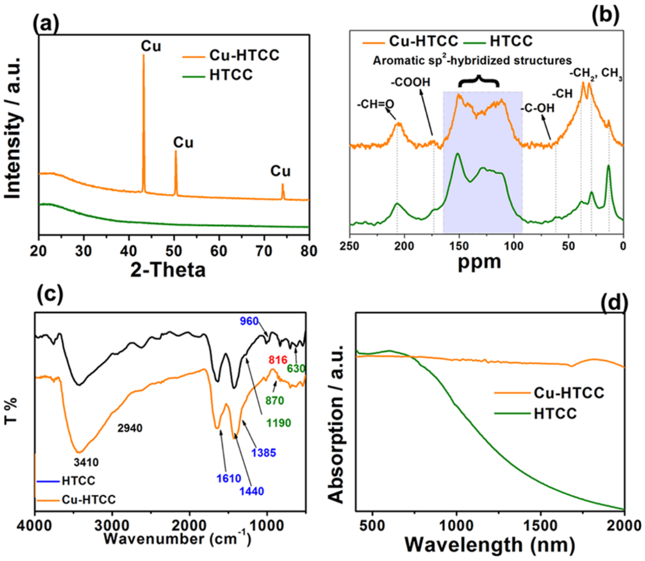

Figure 2. (a) XRD pattern, (b) ^{13}C solid-state NMR spectra, (c) FT-IR spectra, and (d) absorption spectra of HTCC (prepared from glucose) and Cu-HTCC.

The structures of HTCC and Cu-HTCC are studied using the ^{13}C solid-state CP-MAS NMR spectra (Figure 2b). The peaks at 152 and 115−127 ppm correspond to O−C═C and C═C−C of the furan rings, and they are denoted as the polyfuran domains in the spectrum.[41,42] The wide peak centered at 40 ppm can be ascribed to the aliphatic C−H groups. The peaks at 175 and 205 ppm can be assigned to the −COOH and −C═O groups, respectively. These three peaks (40, 175, and 205 ppm) suggest there are some open ring domains in the polyfuran, which is consistent with the result of FT-IR spectra. The ^{13}C solid-state CP-MAS NMR of Cu-HTCC is similar to that of Cu-free HTCC, indicating that the main structure of HTCC remains to be polyfuran. This can also be evidenced by the FT-IR spectra (Figure 2c, Section S2).

The sp^2-hybridized unit of polyfuran is photoactive. Appreciable photocurrents can be generated on both HTCC and Cu-HTCC (Figure S6). Using density function calculation (Figures S7−S9, Section S3), the partial density of states (Figure S8) shows that the sp^2-hybridized units for polyfuran have an obvious band gap, thereby confirming that the polyfuran units can behave like a semiconductor. The absorption spectra of HTCC and Cu-HTCC are compared in Figure 2d. An intrinsic semiconductor-like absorption is also observed in a wide region of HTCC. Its band gap is then estimated to be about 1.3 eV accordingly (Figure S10, Section S5).[21−23] With the addition of Cu, the spectrum of Cu-HTCC shows an apparent plateau in a wide region. This is caused by the absorption of Cu particles because metal often exhibits a wide absorption.

According to density functional calculation (for details, see Section S3), polyfuran chains in pure HTCC are flat, while the polyfuran chains close to the Cu layer are greatly disturbed in Cu-HTCC (Figure S9). This conformation distortion induced by Cu atoms greatly favors the electronic structure of the HTCC. PDOS of polyfuran close to the Cu layer clearly

https://dx.doi.org/10.1021/acsami.0c13323
ACS Appl. Mater. Interfaces 2020, 12, 51366−51373

exhibits the states between the band gap, which makes the band gap smaller and renders the excitation easier (Figure S8).

Photocatalytic CO_2 Reduction Analysis. We prepared HTCC photocatalysts from a series of biomass composite, including glucose, rice, cow dung, and straw. Cu-HTCC is obtained using glucose/$CuSO_4$ or straw/$CuSO_4$. The images shown in Figure 3a,b exhibit the generation rate of CO on different photocatalysts. CO_2 reduction is carried out on a 100 mL home-made reactor (Figure S1), and CO is measured using gas chromatography (for details, see the Experimental Section and Figure S2). A commercial inorganic photocatalyst of TiO_2 (P25) and a typical organic photocatalyst of carbon nitride (C_3N_4) are compared as a reference.

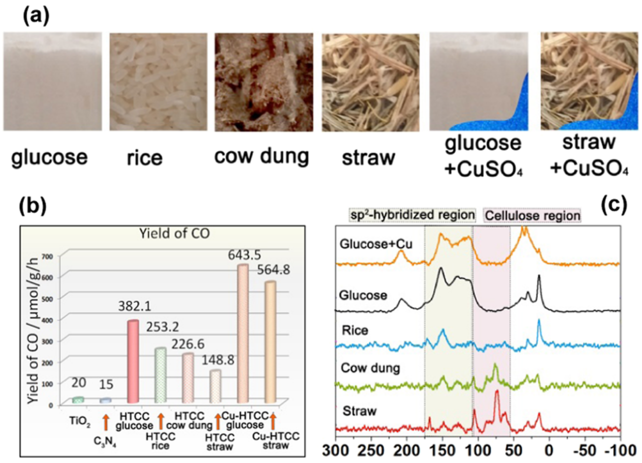

Figure 3. (a) Images of raw materials for HTCC synthesis. (b) Yield of CO from photocatalytic CO_2 reduction on different photocatalysts. (c) ^{13}C solid-state NMR spectra of different photocatalysts, sp^2-hybridized regions, and cellulose regions are denoted using a light yellow and red color.

The activity of TiO_2 for the production of CO is about 20 μmol g^{-1} h^{-1}. Our pure HTCC exhibits a much higher activity of 382.1 μmol g^{-1} h^{-1}. This is 19 times as high as that of commercial TiO_2. This should be partially ascribed to the wider absorption of HTCC (up to 1500 nm) than TiO_2, a semiconductor that only absorbs UV light. The activity of HTCC is also much higher than the typical organic photocatalyst of C_3N_4 (15 μmol g^{-1} h^{-1}). HTCC prepared with other biomasses is also capable of converting CO_2 into CO photocatalytically. HTCC obtained from rice, cow dung, and straw has an activity of 253.2, 226.6, and 148.8 μmol g^{-1} h^{-1}, respectively. With the introduction of Cu, the Cu-HTCC presents the highest activity of 643.5 μmol g^{-1} h^{-1} (Figure 3b). The time profile for yield of CO is shown in Figure S11. Its activity is 32 and 1.7 times higher than that of commercial TiO_2 and pure HTCC, respectively. These values are superior to most of the mainstream photocatalysts reported in the recent years, including TiO_2, C_3N_4, ZnO, $BiVO_4$, and their composites (Table S1).

With the aid of Cu, the Cu-HTCC prepared with straw and $CuSO_4$ also exhibits a high activity of 564.8 μmol g^{-1} h^{-1}, confirming the enhancement of activity by Cu. The solar-to-chemical conversion efficiencies of TiO_2, C_3N_4, HTCC/glucose, HTCC/rice, HTCC/cow dung, HTCC/straw, Cu-HTCC/glucose, and Cu-HTCC/straw are calculated to be 0.06, 0.05, 1.13, 0.75, 0.67, 0.44, 1.91, and 1.68%, respectively (for calculation details, see Section S4). The higher value of Cu-HTCC indicates that the utilization of solar energy for Cu-HTCC is higher. Also, the TOF for HTCC and Cu-HTCC is 0.61 and 0.90 h^{-1} (for calculation details, see Section S4). This indicates that the activity for each active site for Cu-HTCC is better.

Besides, Cu-HTCC prepared with glucose with different purities is also studied and the purity of glucose is found to slightly influence the activity of the samples (Figure S12). The photocatalytic reduction of CO_2 into CO is confirmed by a ^{13}C-labeled isotopic experiment. As shown in Figure 4a, a strong signal at $m/z = 29$ is ascribed to ^{13}CO. This is indicative of the reduction of CO_2 into CO. A controlled experiment is also carried out in the absence of illumination, and no CO is produced. The reason for the activity difference for the sample with different biomasses is further studied. As discussed above, sp^2-hybridized units, like polyfurans, are the main photoactive units in the HTCC. The sp^2-hybridized units are originated from the carbohydrate under hydrothermal conditions. We propose that the activity of the samples is strongly correlated to the content of carbohydrates in the biomass. As shown in ^{13}C solid-state NMR spectra (Figure 3c), the apparent peak of the sp^2-hybridized region at 100−165 ppm can be ascribed to HTCC obtained from the pure carbohydrate of glucose. This peak becomes smaller and smaller in the order of rice > cow dung > straw. Besides carbohydrates, biomasses contain cellulose. As shown in the NMR spectra, the peak of cellulose can be observed in the region of 55−105 ppm. In this region, several overlapped bands relating to C1−C6 (Figure S13) in the unit of cellulose can be found.[43,44] The intensity of the cellulose peak is inverse to the photocatalytic activity. Therefore, the HTCC prepared with carbohydrate-rich biomass exhibits higher activity in photocatalytic CO_2 reduction because the HTCC product contains more photoactive sp^2-hybridized units. Also, the specific surface area is another factor influencing the activity of the samples. The

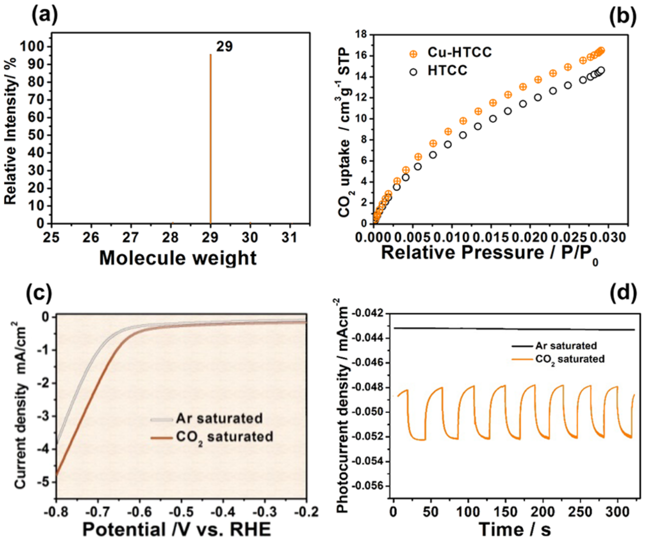

Figure 4. (a) MS spectrum of GC-MS analysis for the CO generated from the $^{13}CO_2$ isotope experiments on Cu-HTCC prepared by glucose and $CuSO_4$. (b) CO_2 absorption curve. (c) Linear sweep voltammetric curves of Cu-HTCC photocatalysts in the dark at 50 mV·s^{-1} in an Ar- or a CO_2-saturated 1 M $KHCO_3$ electrolyte. (d) Photocurrent of Cu-HTCC at −0.6 V vs RHE in an Ar- or a CO_2-saturated 1 M $KHCO_3$ electrolyte.

surface area of HTCC prepared by straw (55.9 m^2/g) is lower than that prepared by pure glucose (92.12 m^2/g). This should be another reason for the lower activity of the sample prepared from straw.

The cycling testing of Cu-HTCC is performed. The photocatalyst maintains 97.6% of its initial activity, suggesting its stability. We believe this stability is acceptable, especially considering the cost of synthesizing these inexpensive photocatalysts and the abundance of its raw material of biomasses.

Adsorption of CO_2 on the photocatalysts is important for its reduction because CO_2 molecules need to be adsorbed on photocatalysts for the following reduction. As shown in Figure 4b, both HTCC and Cu-HTCC exhibit a large uptake of CO_2. In the presence of Cu nanoparticles, the CO_2 uptake increases slightly by 11.7%. Taking a relative pressure of 0.03 as a reference, the HTCC-based photocatalysts exhibit a 9−10 times higher uptake of CO_2 (14−16 $cm^3\ g^{-1}$) when compared with traditional metal oxide photocatalysts of Fe_2O_3 (1.4 $cm^3\ g^{-1}$) and typical carbon nitride (1.7 $cm^3\ g^{-1}$).[45] This higher uptake is ascribed to the presence of a variety of pores from the Cu-HTCC. The BET surface area of HTCC and Cu-HTCC is ca 92.12 and 105.36 m^2/g. BET adsorption−desorption isotherms of Cu-HTCC (Figure S15a) exhibit a typical IV isotherm (based on IUPAC classification).[46] The rapid increase below the relative pressure of 0.1 indicates the existence of lots of micropores, while the hysteretic loop between 0.4 and 0.9 suggests the presence of the mesopores, which is an H4 loop corresponding to the presence of plenty of narrow slits in the HTCC. The presence of micropores and mesopores could be confirmed by the pore-distribution curve (Figure S15b).[46] The micropores and mesopores could accommodate plenty of small CO_2 molecules.

Mechanism of CO_2 Reduction. The mechanism of CO_2 reduction on our samples is investigated by electrochemical measurement, in situ FT-IR spectroscopy, and density functional calculation.

The electrochemical behavior of Cu-HTCC was examined in an Ar- or a CO_2-saturated 1 M $KHCO_3$ electrolyte.[26,27] The linear sweep voltammetry scan is shown in Figure 4c. The curve in CO_2-saturated electrolyte positively shifts by about 0.04 V compared with that in an Ar-saturated electrolyte. This is an obvious indication of CO_2 reduction on the Cu-HTCC. When a photocatalyst is applied at the negative potential in a $KHCO_3$ electrolyte, it is easy to produce a cathodic photocurrent probably due to CO_2 reduction. In our control experiment, TiO_2 exhibits an apparent cathodic photocurrent in a CO_2-saturated $KHCO_3$ electrolyte (Figure S16). With regard to Cu-HTCC, it produces a very small photocurrent at −0.6 V vs RHE in an Ar-saturated electrolyte, while produces appreciable cathodic photocurrent in a CO_2-saturated electrolyte (Figure 4d). This is indicative of its ability to reduce CO_2.

The Tafel plots are obtained according to $\eta = a + b \log|j|$, where η is the overpotential, a is the interception, b is the Tafel slope, and j is the current density (Figures 5a, S17, and S18). The Tafel slope for pure HTCC is 210.3 mV/dec, while that of Cu-HTCC is about 130.3 mV/dec, which is smaller than that of HTCC. This suggests that the addition of Cu is beneficial for the CO_2 reduction. The result of the Tafel analysis of Cu-HTCC is about 130.3 mV/dec, which is close to 118 mV/dec expected for single-electron transfer at the electrode.[47] According to the literature, this suggests that the single-electron transfer is the rate-determining step,[47] suggesting that the absorption of CO_2 is very important for the CO_2 reduction. In situ FT-IR spectra are recorded to investigate the absorption of CO_2 on the surface of the photocatalyst (Figure 5b). The spectrum before the introduction of CO_2 is shown as a dark line in the spectra. After 4 h of illumination in the CO_2atmosphere, the peaks related to COO species (1520 cm^{-1}) monodentate carbonate (1314 and 1543 cm^{-1}) and bicarbonate (1396 and 1421 cm^{-1}) become visible. Obviously, the bidentate carbonate (1651 cm^{-1}) appears remarkable. This peak indicates that the CO_2 is absorbed on the surface by a bidentate model.

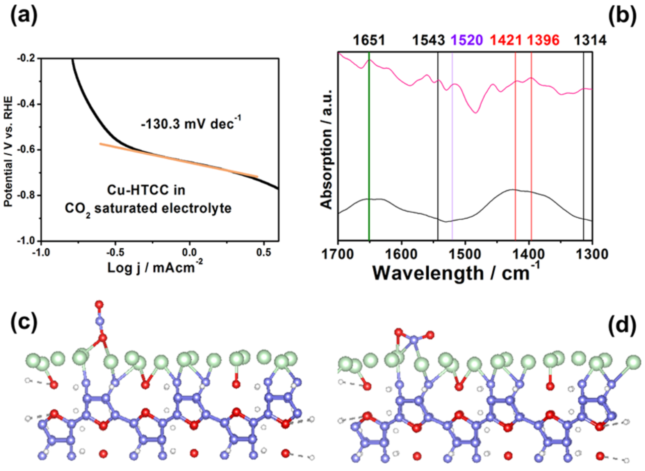

Figure 5. (a) Tafel curve of Cu-HTCC in the CO_2-saturated 1 M $KHCO_3$ electrolyte. (b) In situ FTIR spectra of Cu-HTCC before photocatalytic CO_2 reduction (dark line) and after 4 h of photocatalytic CO_2 reduction (pink line). The structure of CO_2 adsorbed on Cu-HTCC with a perpendicular (c, d) parallel model.

This can be confirmed by our density function calculation. We build two models with CO_2 parallel or perpendicular to Cu-HTCC (Figure 5c,d). The adsorption energy of CO_2 on Cu-HTCC is defined on the basis of the following formula

$$E_{ad} = E_{tot} - E_{substrate} - E_{CO_2} \tag{1}$$

where E_{ad} is the adsorption energy, E_{tot} is the total energy of CO_2-Cu-HTCC, $E_{substrate}$ is the total energy of the Cu-HTCC substrate, and E_{CO_2} is the energy of the CO_2 molecule.

As shown in Table 1, the adsorption energy of CO_2 on the Cu-HTCC substrate is −1.60 and 0.20 eV when it is parallel or perpendicular to the substrate, respectively. The negative value suggests that CO_2 tends to be adsorbed on the substrate by a parallel construction. This is in good agreement with the bidentate model in in situ FT-IR spectra. When adsorbed on CO_2, the C−O bonds (1.160 Å) in the original CO_2 molecule are elongated to 1.199 and 1.194 Å, suggesting the activation of the CO_2 molecule on the substrate of Cu-HTCC.[48]

Table 1. Adsorption Energy of CO_2 on Cu-HTCC when CO_2 is Parallel or Perpendicular to the Substrate

sample	E_{tot} (eV)	$E_{substrate}$ (eV)	E_{CO_2} (eV)	E_{ad} (eV)
perpendicular	604.70	−582.03	−22.88	0.20
parallel	604.98	−582.49	−20.89	−1.60

Function of Cu During Photocatalytic CO_2 Reduction. In a semiconductor and metal photocatalysis system, photoexcited electrons generated in an n-type semiconductor tend to move to the metal because the Fermi level of metal is often lower than the conduction band of semiconductors.[49] In our case, photoexcited electrons tend to migrate from HTCC to Cu. This can be confirmed by the charge difference map (for details, see Section S6, Figure S19). Besides, the charge distributions at different energy levels are studied by the band-decomposed charge density isosurface. As shown in Figure 6a,b, the charge carriers at the energy level of the valance band mainly concentrate on the side of HTCC, while those at the level of the conduction band concentrate on the side of the Cu layer. This suggests that the excitation of charge carriers from the VB to the CB occurs together with the migration of electrons from the HTCC to the Cu layer. This is in good agreement with previous reports, which show that photo-excited electrons migrate from the semiconductor to the metal.[49] In addition, the enhanced charge transfer can be confirmed by the weaker photoluminescence signal due to lower charge recombination (Figure S20).[50]

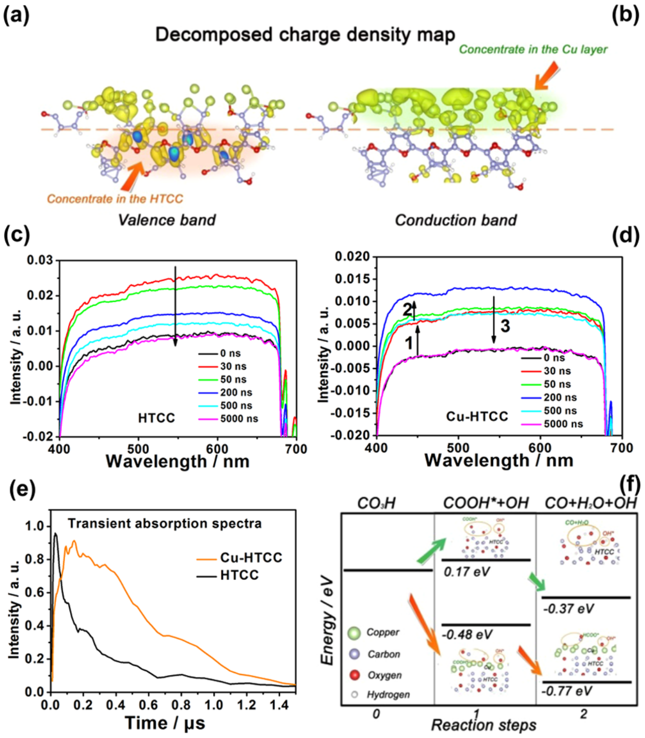

Figure 6. (a) Decomposed charge density isosurface for the valance band (VB) edge and (b) conduction band (CB) edge. Transient absorption spectra of (c) HTCC and (d) Cu-HTCC. (e) Normalized single decay profile. (f) Energy diagram of the two steps during the formation of CO.

The migration of electrons from HTCC to Cu is greatly beneficial to enhance the charge separation in the photocatalytic system. Nanosecond transient absorption spectra (TAS) were recorded to investigate the charge carrier dynamics of HTCC and Cu-HTCC. The spectra were measured using a pump light of 365 nm generated by a Nd:YAG laser. A white light continuum of 450−900 nm was used as the probe light. HTCC can be excited by the pump laser, thereby causing instantaneous excitation of charge carriers from the ground state (GS) to the emission state (EM). As reflected in the TAS curve at different wavelengths (Figure 6c,d), in the beginning (1−30 ns), HTCC exhibits a broad positive signal between 420 and 700 nm, which corresponds to the signal in the EM.[51] With increasing time (30−1000 ns), this peak decays, owing to the recombination of electrons and holes.[52] Cu-HTCC also exhibits a similar trend but the decay occurs later. This excitation-decay process can be observed more clearly in the decay kinetics profile (Figure 6e). The signal initially rises due to pump excitation and decays subsequently after 0.04 μs for HTCC and 0.15 μs for Cu-HTCC. The longer lifetime of the photoexcited electrons in Cu-HTCC suggests that it is more beneficial for photocatalytic CO_2 reduction. The longer lifetime can also be confirmed by the fluorescence lifetime decay, which is discussed in Section S7 and Figure S21.

Coupling with Cu, the decay kinetics curve reaches the top at 0.15 μs, which is 0.11 μs later than that of pure HTCC. Since the component of HTCC in the Cu-HTCC composite has a similar structure as pure HTCC, the kinetics of excited charge carriers should be the same. The decay of the summit peak should be due to the transfer of the photoexcited electrons from the HTCC to the Cu nanoparticles. Migrating to the Cu nanoparticles, the photoexcited electrons have a longer lifetime because their recombination with the photo-excited hole is inhibited. That is why the decrease of the TAS curve of Cu-HTCC is slower than that of pure HTCC.

In addition, as discussed above, the reduction of CO_2 tends to occur on the Cu sides, which is beneficial to the CO_2 reduction because Cu is known to be a good catalyst for CO_2 reduction. We propose that Cu could help to lower the energy barrier of CO_2 reduction. According to the literature, bicarbonate (HCO_3*) species is an important intermediate during CO_2 reduction. It is the primary carbon species after equilibrium on the surface of a catalyst solid. CO_2 reduction often occurs in the electron-accumulated region, which is the active site. Then, CO_2 and OH special are absorbed on the active site to form bicarbonate species.

The formation of CO undergoes the following steps: the first H atom is added to the O atom to form a COOH* species and an OH* species in the first step. Subsequently, the second H atom combines with the COOH* to produce CO, H_2O, and OH*. The final product of OH reacts with another CO_2 to trigger another CO_2 reduction process.

As shown in Figure 6f, on the surface of HTCC, the first step for the formation of CO is thermodynamically unfavorable. The formation of the COOH* intermediate species is endothermic, although the second step is favorable. The formation of CO needs to overcome an energy barrier. On the surface of Cu-HTCC, the cocatalyst Cu greatly promotes the CO_2 reduction. As shown in Figure 6f, the formation of a COOH* intermediate and the generation of CO is preferential to occur, and this formation energy is more negative than that for pure HTCC. This is in good agreement with the higher yield of CO for Cu-HTCC. In conclusion, the presence of Cu promotes charge separation, as confirmed by the charge density analysis. Also, a lower energy barrier of CO formation helps to increase the activity.

CONCLUSIONS

To conclude, the rapid increase of CO_2 in the atmosphere has caused serious global warming and frequently occurring extremely high-temperature weather. Biomasses are one of the most important resources to reduce CO_2 via photosynthesis. However, the direct burning of biomasses releases the fixed carbon into CO_2. This work provides an innovative strategy to transform biomass wastes into HTCC for CO_2 reduction. This study points out a new approach for the utilization of biomasses, especially considering the generation of a huge amount of biomass waste every year. Besides, it is discovered that biomasses can be treated with heavy metals simultaneously to collect heavy metals. The composite products exhibit stronger activity in photocatalytic CO_2 reduction. Therefore, this study provides a new strategy for biomass treatment as well as heavy metal recycling and collection. Biomass is abundant, inexpensive, and easily accessible. The photocatalysts are synthesized from inexpensive biomass, making it easy to obtain and synthesize. This study shows an innovative method to prepared high-efficiency and inexpensive photocatalysts for environmental treatment.

Besides, as most of the metal has a lower Fermi level than an n-type semiconductor of HTCC, it is highly possible that charge separation can be achieved in other metal-HTCC composites. Also, with d-band electrons, many metals can exhibit good catalytic activity. Therefore, they are expected to exhibit good activity as photocatalysts. This study also points out the possibility of preparing other high-efficiency HTCC-based photocatalysts.

■ ASSOCIATED CONTENT

Supporting Information

The Supporting Information is available free of charge at https://pubs.acs.org/doi/10.1021/acsami.0c13323.

Additional information about additional SEM, TEM image, FT-IR spectra, information about the GC analysis of CO, and density functional calculation and TG analysis (PDF)

■ AUTHOR INFORMATION

Corresponding Author

Zhuofeng Hu − *School of Environmental Science and Engineering, Guangdong Provincial Key Laboratory of Environmental Pollution Control and Remediation Technology, Sun Yat-sen University, Guangzhou 510275, China;* orcid.org/0000-0002-7879-6446; Email: huzhf8@mail.sysu.edu.cn

Author

Weiwei Liu − *School of Environmental Science and Engineering, Guangdong Provincial Key Laboratory of Environmental Pollution Control and Remediation Technology, Sun Yat-sen University, Guangzhou 510275, China*

Complete contact information is available at: https://pubs.acs.org/10.1021/acsami.0c13323

Notes

The authors declare no competing financial interest.

■ ACKNOWLEDGMENTS

This work is supported by the National Natural Science Foundation of China (Grant no. 51902357), the Natural Science Foundation of Guangdong Province, China (2019A1515012143), the Start-up Funds for High-Level Talents of Sun Yat-sen University (38000-18841209), the Fundamental Research Funds for the Central Universities (19lgpy153), and the Guangdong Basic and Applied Basic Research Foundation (2019B1515120058). The theoretical calculation is supported by the National Supercomputer Center in Guangzhou and the National Supercomputing Center in Shenzhen (Shenzhen Cloud Computing Center). We thank Dr. Guosheng Li and Miss Xiaoyue zhang for the experiments.

■ REFERENCES

(1) Wang, K.; Li, Q.; Liu, B. S.; Cheng, B.; Ho, W. K.; Yu, J. G. Sulfur-Doped G-C_3N_4 with Enhanced Photocatalytic CO_2-Reduction Performance. *Appl. Catal., B* **2015**, *176–177*, 44–52.

(2) Weng, B. C.; Wei, W.; Yiliguma; Wu, H.; Alenizi, A. M.; Zheng, G. F. Bifunctional CoP and Con Porous Nanocatalysts Derived from Zif-67 in Situ Grown on Nanowire Photoelectrodes for Efficient Photoelectrochemical Water Splitting and CO_2 Reduction. *J. Mater. Chem. A* **2016**, *4*, 15353–15360.

(3) Qin, J. N.; Wang, S. B.; Ren, H.; Hou, Y. D.; Wang, X. C. Photocatalytic Reduction of CO_2 by Graphitic Carbon Nitride Polymers Derived from Urea and Barbituric Acid. *Appl. Catal., B* **2015**, *179*, 1–8.

(4) Wang, S. B.; Wang, X. C. Photocatalytic CO_2 Reduction by Cds Promoted with a Zeolitic Imidazolate Framework. *Appl. Catal., B* **2015**, *162*, 494–500.

(5) Yu, J. G.; Low, J. X.; Xiao, W.; Zhou, P.; Jaroniec, M. Enhanced Photocatalytic CO_2-Reduction Activity of Anatase TiO_2 by Coexposed {001} and {101} Facets. *J. Am. Chem. Soc.* **2014**, *136*, 8839–8842.

(6) Yu, J. G.; Jin, J.; Cheng, B.; Jaroniec, M. A Noble Metal-Free Reduced Graphene Oxide-Cds Nanorod Composite for the Enhanced Visible-Light Photocatalytic Reduction of C CO_2 to Solar Fuel. *J. Mater. Chem. A* **2014**, *2*, 3407–3416.

(7) Wang, S. B.; Yao, W. S.; Lin, J. L.; Ding, Z. X.; Wang, X. C. Cobalt Imidazolate Metal-Organic Frameworks Photosplit CO_2 under Mild Reaction Conditions. *Angew. Chem., Int. Ed.* **2014**, *53*, 1034–1038.

(8) Wang, S. B.; Wang, X. C. Imidazolium Ionic Liquids, Imidazolylidene Heterocyclic Carbenes, and Zeolitic Imidazolate Frameworks for CO_2 Capture and Photochemical Reduction. *Angew. Chem., Int. Ed.* **2016**, *55*, 2308–2320.

(9) Barton, E. E.; Rampulla, D. M.; Bocarsly, A. B. Selective Solar-Driven Reduction of CO_2 to Methanol Using a Catalyzed P-Gap Based Photoelectrochemical Cell. *J. Am. Chem. Soc.* **2008**, *130*, 6342–6344.

(10) Liu, J. Forest Sustainability in China and Implications for a Telecoupled World. *Asia Pac. Policy Stud.* **2014**, *1*, 230–250.

(11) Zhao, B.; Su, Y.; Zhang, Y.; Cui, G. Carbon Dioxide Fixation and Biomass Production from Combustion Flue Gas Using Energy Microalgae. *Energy* **2015**, *89*, 347–357.

(12) Bie, C. B.; Zhu, B. C.; Xu, F. Y.; Zhang, L. Y.; Yu, J. G. In Situ Grown Monolayer N-Doped Graphene on Cds Hollow Spheres with Seamless Contact for Photocatalytic CO_2 Reduction. *Adv. Mater.* **2019**, *31*, No. 1902868.

(13) Xu, F. Y.; Meng, K.; Zhu, B. C.; Liu, H. B.; Xu, J. S.; Yu, J. G. Graphdiyne: A New Photocatalytic CO_2 Reduction Cocatalyst. *Adv. Funct. Mater.* **2019**, *29*, No. 1904256.

(14) Bian, J.; Feng, J. N.; Zhang, Z. Q.; Li, Z. J.; Zhang, Y. H.; Liu, Y. D.; Ali, S.; Qu, Y.; Bai, L. L.; Xie, J. J.; Tang, D. Y.; Li, X.; Bai, F. Q.; Tang, J. W.; Jing, L. Q. Dimension-Matched Zinc Phthalocyanine/Bivo4 Ultrathin Nanocomposites for CO_2 Reduction as Efficient Wide-Visible-Light-Driven Photocatalysts Via a Cascade Charge Transfer. *Angew. Chem., Int. Ed.* **2019**, *58*, 10873–10878.

(15) Zhang, G. G.; Li, G. S.; Heil, T.; Zafeiratos, S.; Lai, F. L.; Savateev, A.; Antonietti, M.; Wang, X. C. Tailoring the Grain Boundary Chemistry of Polymeric Carbon Nitride for Enhanced Solar Hydrogen Production and CO_2 Reduction. *Angew. Chem., Int. Ed.* **2019**, *58*, 3433–3437.

(16) Dong, G. H.; Zhang, L. Z. Porous Structure Dependent Photoreactivity of Graphitic Carbon Nitride under Visible Light. *J. Mater. Chem.* **2012**, *22*, 1160–1166.

(17) Gong, J. M.; Liu, T.; Wang, X. Q.; Hu, X. L.; Zhang, L. Z. Efficient Removal of Heavy Metal Ions from Aqueous Systems with the Assembly of Anisotropic Layered Double Hydroxide Nanocrystals@Carbon Nanosphere. *Environ. Sci. Technol.* **2011**, *45*, 6181−6187.

(18) Niu, P.; Zhang, L. L.; Liu, G.; Cheng, H. M. Graphene-Like Carbon Nitride Nanosheets for Improved Photocatalytic Activities. *Adv. Funct. Mater.* **2012**, *22*, 4763−4770.

(19) Roy, S. Tale of Two Layered Semiconductor Catalysts toward Artificial Photosynthesis. *ACS Appl. Mater. Interfaces* **2020**, *12*, 37811−37833.

(20) Hu, Z.; Yu, J. C.; Ming, T.; Wang, J. A Wide-Spectrum-Responsive TiO_2 Photoanode for Photoelectrochemical Cells. *Appl. Catal., B* **2015**, *168*−*169*, 483−489.

(21) Hu, Z. F.; Shen, Z. R.; Yu, J. C. Converting Carbohydrates to Carbon-Based Photocatalysts for Environmental Treatment. *Environ. Sci. Technol.* **2017**, *51*, 7076−7083.

(22) Wang, T.; Jiang, Z.; An, T.; Li, G.; Zhao, H.; Wong, P. K. Enhanced Visible-Light-Driven Photocatalytic Bacterial Inactivation by Ultrathin Carbon-Coated Magnetic Cobalt Ferrite Nanoparticles. *Environ. Sci. Technol.* **2018**, *52*, 4774−4784.

(23) Wang, T.; Sun, M.; Sun, H.; Shang, J.; Wong, P. K. Efficient Z-Scheme Visible-Light-Driven Photocatalytic Bacterial Inactivation by Hierarchical MoS_2-Encapsulated Hydrothermal Carbonation Carbon Core-Shell Nanospheres. *Appl. Surf. Sci.* **2019**, *464*, 43−52.

(24) Chen, N.; Huang, Y. H.; Hou, X. J.; Ai, Z. H.; Zhang, L. Z. Photochemistry of Hydrochar: Reactive Oxygen Species Generation and Sulfadimidine Degradation. *Environ. Sci. Technol.* **2017**, *51*, 11278−11287.

(25) Chen, N.; Shang, H.; Tao, S. Y.; Wang, X. B.; Zhan, G. M.; Li, H.; An, Z. H.; Yang, J. K.; Zhang, L. Z. Visible Light Driven Organic Pollutants Degradation with Hydrothermally Carbonized Sewage Sludge and Oxalate Via Molecular Oxygen Activation. *Environ. Sci. Technol.* **2018**, *52*, 12656−12666.

(26) Song, Y.; Chen, W.; Zhao, C.; Li, S.; Wei, W.; Sun, Y. Metal-Free Nitrogen-Doped Mesoporous Carbon for Electroreduction of CO_2 to Ethanol. *Angew. Chem., Int. Ed.* **2017**, *56*, 10840−10844.

(27) Bai, X.; Chen, W.; Zhao, C.; Li, S.; Song, Y.; Ge, R.; Wei, W.; Sun, Y. Exclusive Formation of Formic Acid from CO_2 Electroreduction by a Tunable Pd-Sn Alloy. *Angew. Chem., Int. Ed.* **2017**, *56*, 12219−12223.

(28) Kresse, G.; Furthmuller, J. Efficient Iterative Schemes for Ab Initio Total-Energy Calculations Using a Plane-Wave Basis Set. *Phys. Rev. B: Condens. Matter Mater. Phys.* **1996**, *54*, 11169−11186.

(29) Blöchl, P. E. Projector Augmented-Wave Method. *Phys. Rev. B* **1994**, *50*, 17953−17979.

(30) Kresse, G.; Joubert, D. From Ultrasoft Pseudopotentials to the Projector Augmented-Wave Method. *Phys. Rev. B* **1999**, *59*, 1758−1775.

(31) Perdew, J. P.; Burke, K.; Ernzerhof, M. Generalized Gradient Approximation Made Simple. *Phys. Rev. Lett.* **1996**, *77*, 3865−3868.

(32) Bachhuber, F.; von Appen, J.; Dronskowski, R.; Schmidt, P.; Nilges, T.; Pfitzner, A.; Weihrich, R. Van Der Waals Interactions in Selected Allotropes of Phosphorus. *Z. Kristallogr. - Cryst. Mater.* **2015**, *230*, 107−115.

(33) Sun, X. M.; Li, Y. D. Colloidal Carbon Spheres and Their Core/Shell Structures with Noble-Metal Nanoparticles. *Angew. Chem., Int. Ed.* **2004**, *43*, 597−601.

(34) Yu, S. H.; Cui, X. J.; Li, L. L.; Li, K.; Yu, B.; Antonietti, M.; Colfen, H. From Starch to Metal/Carbon Hybrid Nanostructures: Hydrothermal Metal-Catalyzed Carbonization. *Adv. Mater.* **2004**, *16*, 1636−1640.

(35) Peng, L.; Xie, T.; Fan, Z.; Zhao, Q.; Wang, D.; Zheng, D. Surface Photovoltage Characterization of an Oriented A-$Fe2O_3$ Nanorod Array. *Chem. Phys. Lett.* **2008**, *459*, 159−163.

(36) Hu, Z. F.; Chen, C.; Meng, H.; Wang, R. H.; Shen, P. K.; Fu, H. G. Oxygen Reduction Electrocatalysis Enhanced by Nanosized Cubic Vanadium Carbide. *Electrochem. Commun.* **2011**, *13*, 763−765.

(37) Hu, Z. F.; Shen, Z. R.; Yu, J. C.; Cheng, F. Y. Intrinsic Defect Based Homojunction: A Novel Quantum Dots Photoanode with Enhanced Charge Transfer Kinetics. *Appl. Catal., B* **2017**, *203*, 829−838.

(38) Hu, Z. F.; Yan, Z. X.; Shen, P. K.; Zhong, C. J. Nano-Architectures of Ordered Hollow Carbon Spheres Filled with Carbon Webs by Template-Free Controllable Synthesis. *Nanotechnology* **2012**, *23*, No. 485404.

(39) Ding, W.; Yi, Y.; Wang, Y. N.; Zhou, J.; Shi, B. Peroxide-Periodate Co-Modification of Carboxymethylcellulose to Prepare Polysaccharide-Based Tanning Agent with High Solid Content. *Carbohydr. Polym.* **2019**, *224*, No. 115169.

(40) Hu, Z.; Liu, G.; Chen, X.; Shen, Z.; Yu, J. C. Enhancing Charge Separation in Metallic Photocatalysts: A Case Study of the Conducting Molybdenum Dioxide. *Adv. Funct. Mater.* **2016**, *26*, 4445−4455.

(41) del Valle, M. A.; Ugalde, L.; Diaz, F. R.; Bodini, M. E.; Bernede, J. C. Effect of Working Conditions on the Morphology of Electrosynthesized Polyfuran. *J. Appl. Polym. Sci.* **2004**, *92*, 1346−1354.

(42) Hu, J. Z.; Solum, M. S.; Taylor, C. M. V.; Pugmire, R. J.; Grant, D. M. Structural Determination in Carbonaceous Solids Using Advanced Solid State Nmr Techniques. *Energy Fuels* **2001**, *15*, 14−22.

(43) Idström, A.; Schantz, S.; Sundberg, J.; Chmelka, B. F.; Gatenholm, P.; Nordstierna, L. 13c Nmr Assignments of Regenerated Cellulose from Solid-State 2d Nmr Spectroscopy. *Carbohydr. Polym.* **2016**, *151*, 480−487.

(44) Simmons, T. J.; Mortimer, J. C.; Bernardinelli, O. D.; Pöppler, A.-C.; Brown, S. P.; deAzevedo, E. R.; Dupree, R.; Dupree, P. Folding of Xylan onto Cellulose Fibrils in Plant Cell Walls Revealed by Solid-State Nmr. *Nat. Commun.* **2016**, *7*, No. 13902.

(45) Jiang, Z.; Wan, W.; Li, H.; Yuan, S.; Zhao, H.; Wong Po, K. A Hierarchical Z-Scheme A-Fe_2O_3/G-C_3N_4 Hybrid for Enhanced Photocatalytic CO_2 Reduction. *Adv. Mater.* **2018**, *30*, No. 1706108.

(46) Zhuofeng, H.; Zaoxue, Y.; Pei Kang, S.; Chuan-Jian, Z. Nano-Architectures of Ordered Hollow Carbon Spheres Filled with Carbon Webs by Template-Free Controllable Synthesis. *Nanotechnology* **2012**, *23*, No. 485404.

(47) Zhang, S.; Kang, P.; Ubnoske, S.; Brennaman, M. K.; Song, N.; House, R. L.; Glass, J. T.; Meyer, T. J. Polyethylenimine-Enhanced Electrocatalytic Reduction of CO_2 to Formate at Nitrogen-Doped Carbon Nanomaterials. *J. Am. Chem. Soc.* **2014**, *136*, 7845−7848.

(48) Chu, S.; Ou, P.; Ghamari, P.; Vanka, S.; Zhou, B.; Shih, I.; Song, J.; Mi, Z. Photoelectrochemical CO_2 Reduction into Syngas with the Metal/Oxide Interface. *J. Am. Chem. Soc.* **2018**, *140*, 7869−7877.

(49) Sathish, M.; Viswanathan, B.; Viswanath, R. P. Alternate Synthetic Strategy for the Preparation of Cds Nanoparticles and Its Exploitation for Water Splitting. *Int. J. Hydrogen Energy* **2006**, *31*, 891−898.

(50) Dong, W. J.; Yu, H. K.; Lee, J.-L. Abnormal Dewetting of Ag Layer on Three-Dimensional Ito Branches to Form Spatial Plasmonic Nanoparticles for Organic Solar Cells. *Sci. Rep.* **2020**, *10*, No. 12819.

(51) Cioffi, C.; Campidelli, S.; Sooambar, C.; Marcaccio, M.; Marcolongo, G.; Meneghetti, M.; Paolucci, D.; Paolucci, F.; Ehli, C.; Rahman, G. M. A.; Sgobba, V.; Guldi, D. M.; Prato, M. Synthesis, Characterization, and Photoinduced Electron Transfer in Functionalized Single Wall Carbon Nanohorns. *J. Am. Chem. Soc.* **2007**, *129*, 3938−3945.

(52) Pattengale, B.; Ludwig, J.; Huang, J. Atomic Insight into the W-Doping Effect on Carrier Dynamics and Photoelectrochemical Properties of Bivo4 Photoanodes. *J. Phys. Chem. C* **2016**, *120*, 1421−1427.